Soft Matter

Accepted Manuscript

This is an *Accepted Manuscript*, which has been through the Royal Society of Chemistry peer review process and has been accepted for publication.

Accepted Manuscripts are published online shortly after acceptance, before technical editing, formatting and proof reading. Using this free service, authors can make their results available to the community, in citable form, before we publish the edited article. We will replace this *Accepted Manuscript* with the edited and formatted *Advance Article* as soon as it is available.

You can find more information about *Accepted Manuscripts* in the Information for Authors.

Please note that technical editing may introduce minor changes to the text and/or graphics, which may alter content. The journal's standard Terms & Conditions and the Ethical guidelines still apply. In no event shall the Royal Society of Chemistry be held responsible for any errors or omissions in this *Accepted Manuscript* or any consequences arising from the use of any information it contains.

ROYAL SOCIETY OF CHEMISTRY

www.rsc.org/softmatter

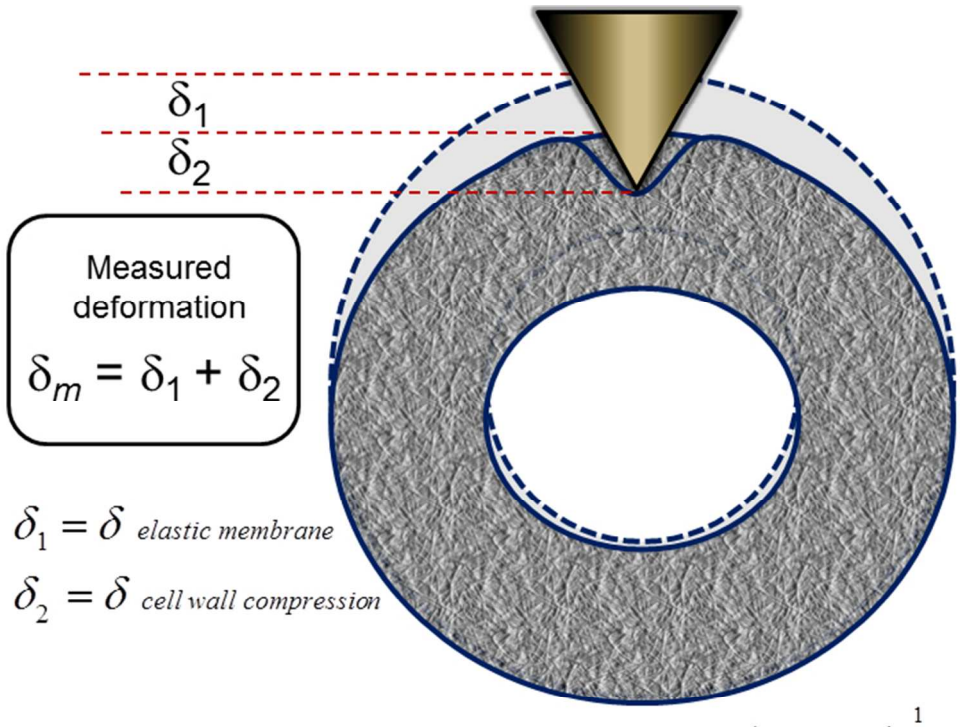

$$\delta_m = \sum_{i=1}^{N} \Theta(F_m - F_0 - F_{lc,i})\Theta(F_{uc,i} - F_m + F_0)\left(\frac{F_m - F_0}{k_i}\right)^{\frac{1}{n_i}}$$

$$+ \sum_{i=1}^{N} \Theta(F_m - F_0 - F_{uc,i})\left(\frac{F_{uc,i}}{k_i}\right)^{\frac{1}{n_i}} + \delta_0$$

The graphic illustrates different types of deformation that occurring during indentation of a plant cell, including cell wall compression and membrane deflection. It also shows that the total measured deformation is a convoluted quantity, that we are seeking to find through the use of our new Multi-Regime Analysis method, the mathematical gist of which is illustrated by the formula at the bottom of the figure.
192x190mm (96 x 96 DPI)

Soft Matter

RSCPublishing

ARTICLE

Interpreting Atomic Force Microscopy Nanoindentation of Hierarchical Biological Materials using Multi-Regime Analysis

Cite this: DOI: 10.1039/x0xx00000x

Received ooth January 2012,
Accepted ooth January 2012

DOI: 10.1039/x0xx00000x

www.rsc.org/

M.R. Bonilla,[a] J. R. Stokes,[ab] M.J. Gidley[c] and G. Y. Yakubov*[a]

We present a novel Multi-Regime Analysis (MRA) routine for interpreting force indentation measurements of soft materials using atomic force microscopy. The MRA approach combines both well established and semi-empirical theories of contact mechanics within a single framework to deconvolute highly complex and non-linear force-indentation curves. The fundamental assumption in the present form of the model is that each structural contribution to the mechanical response acts in series with other 'mechanical resistors'. This simplification enables interpretation of the micromechanical properties of materials with hierarchical structures and it allows automated processing of large data sets, which is particularly indispensable for biological systems. We validate the algorithm by demonstrating for the first time that the elastic modulus of polydimethylsiloxane (PDMS) films is accurately predicted from both approach and retraction branches of force-indentation curves. For biological systems with complex hierarchical structures, we show the unique capability of MRA to map the micromechanics of live plant cells, revealing an intricate sequence of mechanical deformations resolved with precision that is unattainable using conventional methods of analysis. We recommend the routine use of MRA to interpret AFM force-indentation measurements for other complex soft materials including mammalian cells, bacteria and nanomaterials.

1 Introduction

Atomic force microscopy (AFM) is widely used for nanoindentation to characterise the micromechanics of complex biological systems including cells. [1] The attraction of using AFM for nanoindentation is its ability to measure very low forces and its operational versatility, as well as the potential to include in-situ imaging. An appropriate contact mechanical model is needed to interpret force-indentation curves (FIC), the particular choice of which requires an expert knowledge of the system under scrutiny and awareness of the chosen model's limitations. This is challenging for systems that exhibit highly non-linear mechanical responses and for biological materials that are heterogeneous and comprise a number of morphological features, each having unique micro-mechanical properties. A further challenge in regards to using AFM for nano-indentation is the uncertainty of the true contact area and the absolute surface separation between probe and sample. Thus, the central displacement values during the

indentation are also uncertain, which inhibits quantitative interpretation of experimental data. Here, we present a simple algorithm that tackles these challenges and allows analysis and interpretation of complex force-indentation curves such as those collected on plant cells. [2, 3] The algorithm is implemented into an automated routine, which is essential for heterogeneous biological materials that require an extensive number of measurements for establishing statistical significance. The approach can be equally applied to characterising the micromechanics of a broad range of soft materials using the AFM, including mammalian cells, bacteria and nanomaterials such as polyelectrolyte multilayer capsules. [4]

In practice, the commonly used approaches for analysing AFM nanoindentation data rely on choosing a segment of the force-distance curve, in which reasonable assumptions can be made with regards to compatibility with a chosen mechanical model.[5] For example, it is typical to analyse only those segments of a FIC where the force (F) is a power law function of the indentation (δ), which is consistent with the Hertzian small deformation approximation: $F \propto \delta^{3/2}$ for a spherical probe or $F \propto \delta^2$ for a conical indenter such as an AFM tip. Variations from a power-law response are usually accommodated by refining the model to account for specific system properties and measurement conditions. The Hertzian theory of contact deformation is among the most widely used and has received numerous modifications to account for: anisotropic material properties [6] and multi-layered structures; [7] finite thickness of tested films and the presence of supporting substrate; [8, 9] large deformations; [10] adhesive interactions; [11-15] and viscoelastic behaviour. [12, 16-18]

Despite the variety of contact mechanics models available, a complication with interpreting AFM data stems from the fact that indentation is convoluted with surface forces, which renders determination of the position of zero-indentation difficult unless surface forces are explicitly included into the model. [19, 20] In biological systems, due to the weakness of DLVO forces, the surface interactions are typically dominated by steric forces associated with surface bound polymers. In mammalian cells, these can be glycocalyx mucins or polymeric species adsorbed from the media, while for plant and bacterial cells, these are cell wall polysaccharides and proteoglycans. Usually little is known about the exact nature of such polymeric layers in biological systems as their composition typically exhibits microheterogeneity, [21] and hence it cannot be easily accounted for using established theories like those used to describe the micromechanical properties and surface forces associated with well-defined polymer brushes. [22]

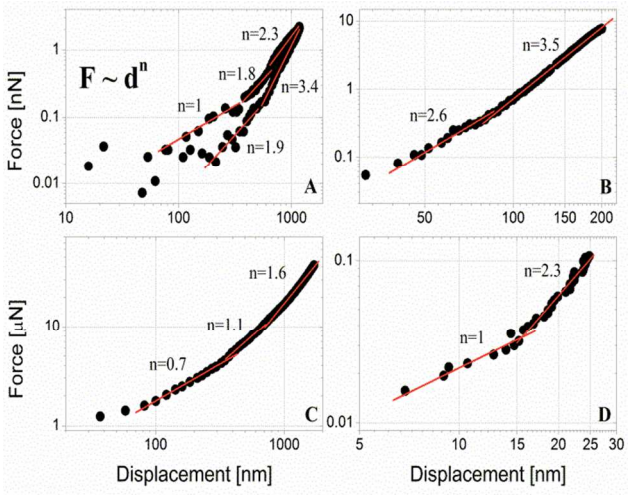

Figure 1. Characteristic indentation curves of (A) bovine cartilage, [23] (B) bovine ovary, [24] (C) yeast, [25] and (D) cactus spine [26] cells. FICs (A), (B) and (D) were obtained through a conical AFM tip, while FIC (C) was obtained through a 50 μm diameter flat indenter. Despite the differences in the magnitude of the forces and indenter geometry, all FICs display a characteristic multi-linear shape in logarithmic scale, suggesting that in different sections of the curve a dominant power-law regime dictates the force (F) – displacement (d) relationship. The value of the slope n provides valuable information on the physical mechanisms in action. Reproduced with permission.

The Oliver-Pharr (OP) model is used to avoid the influence of the surface forces and to mitigate the uncertainty of the true contact area when interpreting FICs. [27] This model established an analytical relationship between the Hertzian elastic modulus and the slope of the initial part of the unloading curve, where it is assumed that the contact area stays constant. The OP model gained significant popularity due to its simplicity, analytical form, and ease of implementation in the form of an automated routine for processing large arrays of FICs. It has also been implemented in the majority of commercial AFM software packages. However, applicability of the OP model is confined to contacts that behave within the Hertzian approximation, and it cannot be used for any arbitrary curve without adequate controls. There is thus a strong impetus to

develop a simple algorithm (as an opposite to a full numerical simulation) that can be used to interpret FICs where the choice of appropriate micromechanical model is ambiguous.

The new Multi-Regime Analysis (MRA) developed here is based on the fact that the FICs of many soft materials display a characteristic multi-linear shape when graphed in logarithmic scale, as depicted in Figure 1 for bacterial, mammalian and plant cells. Every linear section of the curve is associated with a dominant power-law relationship between force F and indentation depth d, the exponent of which can be identified with a particular regime through a preliminary histogram analysis followed by an optimization procedure. The new algorithm maximizes the extraction of quantifiable information convoluted within force indentation measurements, whilst ensuring that force analysis complies with assumptions and applicability limits of mechanical models. The adequacy of the automated routine is demonstrated by characterizing the complex micromechanical properties of heterogeneous plant cells from *Lolium multiflorum* cell culture. We show also that this new approach enhances the accuracy of nanoindentation measurements on model elastomer surfaces. Moreover, the qualitative similarity between the FICs in Figure 1 arising from their multi-regime nature allows us to suggest that MRA can be employed to interpret indentation data on other complex systems.

2 Materials and methods

2.1 Colloidal probe preparation

Colloidal probes were fabricated in house using glass beads (30-50 µm diameter) and Polybead™ polystyrene microspheres (diameter 10.52 µm) both from Polysciences (Polysciences Inc., PA). Spheres were attached on the top of the AFM cantilever using epoxy glue (UHU GmbH & Co. KG, Germany) and cured at room temperature (24°C) for at least 72 hours. Before use, probes were cleaned in oxygen plasma for 5 min, and immediately after cleaning they were mounted in the holder and immersed in the experimental cuvette with buffer. In addition to colloidal probes, the following pre-manufactured AFM tips were used; PNP-TR Si_3N_4 (R<10 nm) from NanoWorld (NanoWorld AG, Germany), DNP Si_3N_4 (R~20 nm) from Bruker (Bruker AFM Probes, CA), and NSC/CSC Si tips (R<10 nm) from Mikromasch (NanoWorld AG, Germany). For colloidal probes, several tipless cantilevers were used including: CSG 11 (gold coated) from NT-MDT (NT-MDT, Russia), and CSC 37/NSC 36 (Al coated) from MikroMasch (NanoWorld AG, Germany). The spring constant (k) of the sensors ranged from 0.05 up to 1 N/m, and was determined using the Asylum Research GetReal™ routine that utilises a combination of the thermal noise and the Sader methods [28, 29]. The geometric parameters of the probes were obtained from analysis of scanning electron microscope (SEM) microphotographs.

2.2 *Lolium multiflorum* Suspension Culture Cells

L.multiflorum suspended culture cells were used as a model biological system with complex mechanical properties. The culture was derived from the endosperm of *Lolium multiflorum* grown in 250 ml Erlenmeyer flasks containing 150 ml of modified White's medium [30] (ionic strength 0.435 mol/l, osmotic pressure 1.17 MPa). The cultures were maintained in the dark at 27°C with constant shaking at 130 rpm. Sub-cultures were conducted every 10 days by weighing 30 g (fresh weight) of cells and transferring the cells to 150 ml of fresh medium.

Prior to conducting AFM measurements, the suspensions were sieved to isolate small cell clusters and individuals cells. Sieving was performed using steel mesh sieves (ISO 3310 Test Sieves, Essa, Australia). Firstly, a sieve with 300 µm mesh was used; the filtrate was then passed through the sieve with 90 µm mesh. An additional volume of media was used to facilitate the penetration of the cell slurry through the mesh. Two volumes of media was used for sieving cell suspensions. After sieving, the suspensions were transferred to the measuring apparatus within 2 hours.

2.3 PDMS preparation and bulk mechanical tests

Two component polydymethilsiloxane (PDMS) (SYLGARD® 184 Silicon Elastomer Kit, Dow Corning, MI) substrates were prepared by casting. The Young's modulus of the PDMS was measured through uniaxial extension using the Instron MicroTester (MicroTester

model 5848, Instron, MA) as well as using a Texture analyser (TA.XTplus, Stable Micro Systems, United Kingdom) and was found to be 1.45±0.5MPa [31]. To minimise adhesion, PDMS sheets were treated using oxygen plasma (Expanded Plasma Cleaner PDC 001/002, Harrick Plasma, NY) to render them hydrophilic. The samples were held in a vacuum at a vapour pressure of 0.2mbar, and a current of 15mA was applied for 30 seconds; after treatment the samples were immediately immersed in water and used at once.

2.4 AFM measurements

AFM measurements were conducted using a JPK Nanowizard II AFM mounted on an inverted optical microscope (JPK Instruments, Germany) for measurements of cells using a CellHesion controller with a Z-piezoelectric translator range of 100 µm. A MFP-3D-BIO AFM mounted on an inverted optical microscope (Asylum Research, CA) was used to conduct measurements on PDMS substrates. All measurements were performed in the closed loop mode. Indentation curves were recorded using driving speeds ranging from 200 nm/s up to 1 µm/s; the value depended on the radius of the probe so as to minimise the impact of hydrodynamic drag that at all times was less than 5Å in the deflection equivalent[32, 33]. The total Z-piezo travel distance was typically from 1.5 to 3 µm, and zero dwell time was selected between approach and retraction branches. This allowed the contact time between tip and substrate to be less than 2 seconds. To convert the output voltage of the position sensitive device to a deflection in nanometers, we calculated the slope of the constant compliance line measured prior to and after the measurements in the same buffer/solvent by recording the force curves against a glass/Si wafer substrate. The force was calculated by multiplying deflection by the cantilever spring constant. The zero position was determined as the cross-section point of the baseline and the tangent line corresponding to the onset of the indentation curve, where cantilever deflection started to deviate from the baseline. Positive values were attributed to the indentation section of the curve. The apparent separation was calculated by subtracting cantilever deflection from the *z*-position of the piezotranslator. Such processed indentation/surface force curves were used for further analysis. No further assumption has been made with regards to whether the low deflection sections of the FIC correspond to surface forces or actual indentation.

Measurements on cells were carried out in the same buffer used for cell culture after filtering it twice through a 0.2 µm pore size membrane filter (MillexGS MCE, Millipore, Ireland). Upon immersion into buffer solution the system was thermostated for typically 20-40 minutes to ensure minimal cantilever drift. All probe surfaces were considered to be hydrophilic (after plasma treatment) and microparticles were found to have a RMS surface roughness below 0.3nm over an area of 1 µm^2.

Figure 2 shows a *L. multiflorum* cell confined within a PDMS microwell [34] that is indented using an AFM tip. To avoid cell damage and minimize plastic deformation due to prolonged contact, the maximum indentations were limited to 500 nm, and maximal forces to 150 -200 nN, which is adequate for plant cells which are much stiffer and larger than mammalian cells. [35]

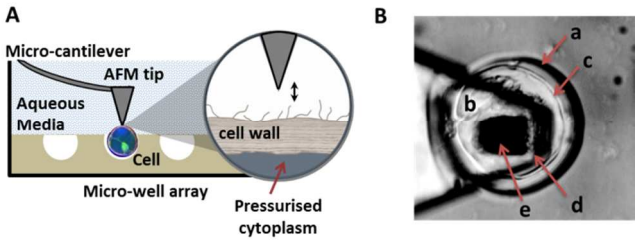

Figure 2. (**A**) Schematic diagram of indentation experiments using *Lolium multiflorum* cells confined within PDMS microwells. The zoomed-in sketch represents the complex layered structure of the cell surface, where the multi-regime nature of the elastic response originates. (**B**) A dual illumination (Bright-Field and Reflected Light) optical micrograph of a *L. multiflorum* cell (b) confined within a PDMS micro-well (a). An AFM cantilever (d) is positioned above the cell so that the tip (e) is positioned approximately above the apex of the cell. The cell wall (c) can be clearly visualised as a shell surrounding the cell.

3 Results and discussion

3.1 Theoretical framework for a Multi-Regime Analysis (MRA)

Figure 3 presents typical FICs for a *L.multiflorum* cell (A) and PDMS elastomer (B) recorded using a conical tip and a colloidal probe respectively. Most contact mechanics models predict that the force is a power-law function of the central displacement, i.e. $F \propto \delta^n$, therefore it is more

convenient to display data in logarithmic coordinates. On a logarithmic scale (Figure 3, bottom panels), the experimental FICs frequently show two or more distinct power law regimes, with power law exponents for these regimes deviating from the expected Hertzian values of n=3/2 for a sphere and n=2 for a cone/pyramid.

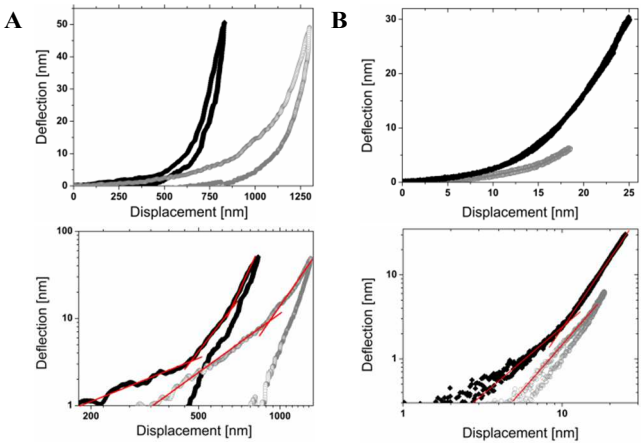

Figure 3. (A) Typical force versus indentation curves for a *L. multiflorum* suspension cell recorded using AFM tip (R ~ 20 nm) and soft cantilever (~30 pN/nm). (B) Typical force versus indentation curves for PDMS elastomer recorded using a colloidal probe (R = 5.16±0.13µm) and moderately stiff cantilever (0.825±0.005 nN/nm). The logarithmic plots show empirical power law fits of different sections of the curve and illustrate the empirical basis of the Multi-Regime Analysis.

We note that each power law regime spans across a considerable range of indentation values, and therefore should be attributed to a consolidated set of deformations that dominate mechanical behaviour. To confirm this observation, i.e. that significant sections of FICs are characterized by the same slope; we have performed linear fitting (in log-log coordinates) of short segments of FICs, with gradients used to construct a frequency histogram. The individual histograms are then averaged to yield a spectrum of power law exponents.

To illustrate the method we will use results obtained for the *L.multiflorum* cells, the wall of which displays a clear hierarchical structure. In contrast to mammalian cells, the phospholipid plasma membrane in plant cells is surrounded by a stiff wall containing cellulose fibres (Figure 2A). The cell wall restricts the expansion of turgid cells, in a similar fashion to how the tough rubber of a bicycle tire provides a limit to the pumping of air into an elastic inner tube. During an indentation cycle, both the cell wall and the cell wall shell (shown as a spherical membrane in Figure 4A) deform. In Figure S3 of the Supplementary Information, a typical spectrum of power law exponents obtained for *L.multiflorum* cells is presented that suggests the presence of five dominant regimes. The position of the main maximum deviates from the value of 2 expected for a Hertzian contact exerted by an AFM tip. This deviation does not necessarily mean that the Hertzian model is not appropriate, since neither the contact area nor absolute deformation is known. [36] Deviation from the Hertzian model may also arise because deformations of different structures within the cell are convoluted within a single FIC; as illustrated in Figure 4A for plant cells. The total indentation in this example comprises two contributions; one is from the compression of the cell wall, and another from the deflection of a spherical shell. If we assume both structures deform elastically, a constitutive model can be defined by considering the system to be a set of springs connected in series (Figure 4B). [37]

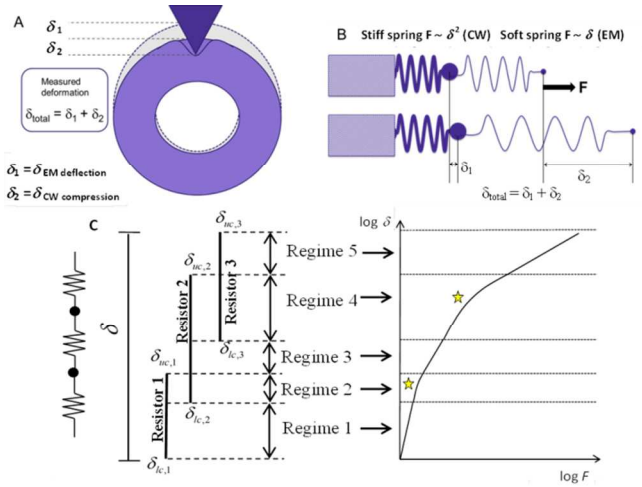

Figure 4. (**A**) The schematics of plant cell wall deformation during indentation with an AFM tip, and(**B**) the corresponding spring model, illustrating a scenario where cell wall (CW) compression and elastic membrane (EM) deflection are convoluted. (**C**) Generalization of a multi-resistors system: a sketch of three resistors in series with their ranges of action overlapping to produce five different elastic regimes. The FIC on the right has the combination of resistors shown on the left side. The regimes labelled with a star are the product of the simultaneous action of two resistors and cannot be represented by a single slope in the log-log plot. Instead, the slope evolves continuously from the characteristic power law exponent of one resistor to the

other.

To generalize this approach, the cantilever deflection is assumed to be the result of N elastic resistors in a series at any given point on an indentation curve, as illustrated in Figure 4C. The restoring force for the i th resistor, F_i, relates to its corresponding deformation, δ_i, by a law of the form of equation (1). For a quasi-static system in series, the restoring force is the same for all resistors, i.e. $F_i = F_j = F$ for all i, j; moreover, the total deformation δ is the summation of the individual deformations (equation (2)), which means that the FIC can be found as the solution to the system of N equations with N unknowns (equation (3))

$$F_i = f_i(\delta_i^{n_i}, \delta_i^{n_i-1}, ..., \delta_i) = f_i(\delta_i, n_i) \quad (1)$$

$$\delta = \sum_{i=1}^{n} \delta_i \quad (2)$$

$$f_i(\delta_i, n_i) = f_{i+1}(\delta_{i+1}, n_{i+1}); \quad i = 1, ..., N-1 \quad (3)$$

Let us define δ_m and F_m as the experimentally measured values of deformation and force, respectively, and δ_0 and F_0 as the corresponding measurements at zero deformation (i.e. $\delta_0 = \delta_m - \delta_0$ and $F = F_m - F_0$). For a simple power law of the form $f_i(\delta_i, n_i) = k_i \delta_i^{n_i}$, the above system of equations can be rearranged into a linear form as a superposition of individual deformations with $2N$ system parameters, $\delta = \sum_{i=1}^{N} (F_i / k_i)^{1/n_i}$. Due to the intrinsic uncertainty in determining the zero indentation and zero force using the AFM, we – following existing approaches [38, 39] - include the offsets in this expression to obtain

$$\delta_m = \sum_{i=1}^{N} \left(\frac{F_m - F_0}{k_i} \right)^{\frac{1}{n_i}} + \delta_0 \quad (4)$$

If the force-deformation relationship for resistor i has a more general power law form, say $f_i(\delta_i, n_i) = \sum_{j=1}^{n_i} k_{j,i} \delta_i^{n_i - j + 1}$ (which applies to the deformation of a thin film [8, 9]), it is possible to determine $\delta_i(F)$ by simple interpolation (see Section S3 of Supplementary Information for details).

In general, not all elastic resistors deform over the whole range of measured deformations, but it is possible that an upper critical deformation $\delta = \delta_{uc,i}$ exists for resistor i such that, for $\delta > \delta_{uc,i}$ resistor i ceases to deform and does not further contribute to change of the total elastic force. A lower critical deformation $\delta = \delta_{lc,i}$ may also exist for resistor i such that, for $\delta < \delta_{lc,i}$, resistor i displays infinite stiffness and cannot be deformed. Fig. 4C depicts a schematic arrangement of three resistors in series and a diagram showing how overlap of their ranges of action creates five different elastic regimes. The use of critical deformations is an approximation that can be computationally solved using a system of recurrent equations. For example, if resistors 2 and 3 are acting in regime 4, then for this regime ($\delta_{lc,3} \le \delta \le \delta_{uc,3}$) the following relation is obtained for the experimentally measured indentation:

$$\delta_m = \delta_{lc,3} + \Delta\delta = \delta_{lc,3} + \Delta\delta_2 + \Delta\delta_3 \quad (5)$$

Where $\Delta\delta$ and $\Delta\delta_i$ are the total deformation and that corresponding to resistor i only from the onset of regime 4. Hence for this regime one can show that:

$$f_3\left(\delta_m - \left(\delta_{lc,3} + \Delta\delta_2\right)\right) = F^{(3)} + f_2\left(\delta_{lc,3} + \Delta\delta_2\right) - f_2\left(\delta_{lc,3}\right) \quad (6)$$

Where $F^{(3)}$ is the maximum force experienced in the preceding regime (regime 3 in this example). If resistors 2 and 3 can be described using a simple power law model ($f_i(\delta_i, n_i) = k_i \delta_i^{n_i}$), then the system of equations (5) and (6) can be solved analytically, yielding

$$\delta_m = \left(\frac{F_m}{k_3}\right)^{1/n_3} + \left(\frac{F_m - F^{(3)}}{k_2} + \delta_{lc,3}{}^{n_2}\right)^{\left(1/n_2\right)} \quad (7)$$

Since all parameters in equation (7) except k_3 and n_3 are already determined in the previous regime, the new regime has only 2 unique fitting parameters. The algorithm therefore limits the number of fitting parameters for each segment of the curve. At the same time it enables modelling of complex curves with multiple regimes to be described by different physical models. In addition, this approach enables capture of the transitional regions, and therefore can simulate deformations with a wide range of power law exponents.

Critical limits can also be defined in terms of forces ($F_{lc,i}$ and $F_{uc,i}$) instead of deformations as long as a one-to-one relationship between $F_{lc,i}$ - $\delta_{lc,i}$ and $F_{uc,i}$ - $\delta_{uc,i}$ holds. In such case, for N power law resistors the measured indentation will be given by:

$$\delta_m = \sum_{i=1}^{N} \Theta(F_m - F_0 - F_{lc,i})\Theta(F_{uc,i} - F_m + F_0)\left(\frac{F_m - F_0}{k_i}\right)^{\frac{1}{n_i}} + \sum_{i=1}^{N} \Theta(F_m - F_0 - F_{uc,i})\left(\frac{F_{uc,i}}{k_i}\right)^{\frac{1}{n_i}} + \delta_0 \quad (8)$$

where $\Theta(x)$ is the Heaviside function, taking the value zero for $x < 0$ and unity otherwise. The last term on the right hand side of equation (8) stems from the fact that resistors above their critical limit at the given force contribute to the total deformation with their maximum deformation. Interpolation extracts $\delta_i(F)$ for resistors following more complex functional forms, switching the regimes on or off appropriately through the use of Heaviside functions (See section S3 of Supplementary information).

3.2 Implementation of automated routine

The modelling procedure was implemented in MATLAB. In order to enable the fitting of experimental data with deformations spanning over several decades, an appropriate re-scaling was introduced. Since our analysis is based on observation of the multi-regime nature of the log-log curves, it is more appropriate in this case to re-state the objective function J for the fitting procedure in terms of the logarithm of the displacements, as:

$$J = \sum_j \left(\log \delta_{m,j}^{\text{pred}} - \log \delta_{m,j}^{\text{exp}}\right)^2 + \alpha N_r + \beta N_p \quad (9)$$

The superscripts "*pred*" and "*exp*" stand for predicted and experimental values, respectively. Large deformations will have a higher weight during the fitting process than small ones, which is desirable as large deformation are associated with smaller relative measurement errors; however, the difference in the weight between large and small deformations is considerably smaller than it would be if the sum was taken over $\left(\delta_{m,j}^{\text{pred}} - \delta_{m,j}^{\text{exp}}\right)^2$. Penalties for combinations of resistors generating a large number of regimes or large sets of fitting parameters are added through the last two terms on the right hand side, where N_r and N_p are number of regimes and fitting parameters, respectively, and α and β appropriate weights. Nevertheless, performing curve fitting in linear scale is a convenient cross-validation method that adequate regimes and parameters are being produced, as discussed in Section S4 of the Supplementary Information.

Given the large number of parameters resulting from fitting of a single curve, the likelihood that a non-unique set of parameters locally minimizes the objective function J is high. In order to reduce the computational burden and improve consistency, the pre-selection of at least one resistor for which $\delta_{lc,i} = 0$ (or $F_{lc,i} = 0$) and one resistor for which $\delta_{uc,i} = \delta_{max}$ (or $F_{uc,i} = F_{max}$) is convenient. For most biological and soft materials, the regime with $\delta_{lc,i} = 0$ corresponds to surface roughness (partial contact) and/or the presence of a loose layer of polymer chains protruding from the core material. High values of the power law exponent, n, are usually associated with large deformation behavior (i.e. when approaching the linear limit of the AFM cantilever spring) and, as a consequence, it is likely that the elastic resistor with highest n has δ_{max} as its upper critical limit. Again, this does not mean that another resistor cannot have δ_{max} as its upper critical limit. Setting these two "boundary" resistors in advance avoids fitting with an otherwise difficult restriction.

3.3 Complete FI curve modelling of a model elastomer

In order to validate the methodology, we studied micromechanical properties of PDMS elastomer. PDMS has complex micromechanical properties due to partial penetration of water into the material[40], viscoelastic properties associated with uncrosslinked silicone polymer still present in the material,[18] as well as possible changes within the surface layer associated with plasma treatment. Nevertheless, in the applied load and speed range the response was essentially elastic, producing negligible hysteresis. We chose PDMS because it has been extensively studied before using nanoindentation[41, 42] and its bulk mechanical modulus is measurable using alternative methods. In addition, the expected values for the elastic modulus of PDMS elastomer are of the order of a few MPa, which matches juvenile plant cells that are of interest here. Thus Milani et al. [43] measured a modulus of ~5 MPa and ~1.5 MPa for respectively the tip and flank cells of the shoot apical meristems of *Arabidopsis thaliana*. The modulus may be higher (10-100 MPa)[44, 45] for other types of plant cells, while for mammalian cells it can be as low as a few kPa[46]. This, however, does not change the principle of the applied analysis, although the exact choice of deformation regimes should be tailored for each individual system.

In order to illustrate the use of MRA for the extraction of mechanical parameters the procedure described in the previous section is followed in detail for the analysis of indentation of PDMS with a 10 μm radius spherical probe. Figure 5 combines the approach histograms of 5 different indentations. Here, along with major peaks between the slopes 2 and 3 (indicative of an elastic thin film), minor peaks are noted between slopes 0-1 and 1-2, corresponding to surface interactions (including possible uncertainties in δ_0 and F_0) and Hertzian elastic response. The lack of major peaks above a slope of 4.5 makes it reasonable to discard contributions from non-linearity of cantilever deflection (i.e. hyperelastic regime).

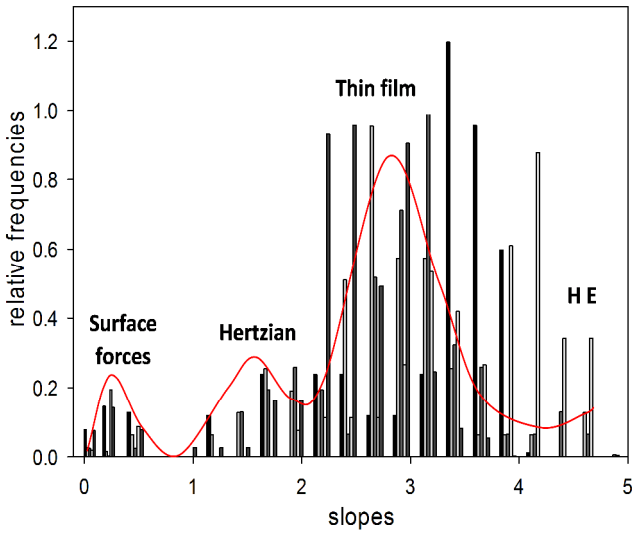

Figure 5. Selected histograms of the approach branch for five FICs (bars) of PDMS using a 10.5 μm diameter spherical indenter and the best fit using a combination of Gaussians (red line). The individual histograms display the concurrent contribution of several regimes. Hyperelasticity (HE) effects are relatively minor and will not be considered in the fitting process.

From the information provided by the histograms, three different resistors are considered:

1) Polymer steric repulsion model (equation (S.1)), n <1;
2) Hertzian-Sneddon model (HS), (equations (S.3)-(S.4)), n = 3/2 for a sphere;
3) Thin film elastic model developed by Chadwick and co-workers (HC) as a series expansion with power law terms with exponents n = [3/2, 2, 5/2, 3, 7/2] for a sphere (equation (S.5))

The lower critical limit for resistor 1 is $\delta_{lc,1} = 0$, while the upper critical limit for resistor 3 is set to $\delta_{uc,3} = \delta_{max}$. The fitting parameters arising from the resistor models are k_p, n_p, h, E_{eff}^{HS} and E_{eff}^{HC}, where superscripts HS and HC indicate Hertzian-Sneddon or Hertzian-Chadwick, respectively. One scenario in which resistors 2 and 3 coexist within the same regime is that in which thin film and substrate deform concomitantly to a sufficient degree that the substrate contribution is significant. Additional fitting parameters are the critical limits $\delta_{lc,2}$, $\delta_{lc,3}$, $\delta_{uc,1}$, $\delta_{uc,2}$ and the offsets in force and indenter displacement, δ_0 and F_0. It is entirely possible that regime i is not present, i.e. $\delta_{lc,i} = \delta_{uc,i}$. Given the structure of the objective function this scenario will be slightly favored, as it leads to a reduction in the number of regimes, N_r and parameters, N_p.

Table 1. Model parameters obtained through MRA for the fitting of the FIC in Figure 6.

Parameter	value
δ_0	2.07 nm
F_0	0.53 nN
k_1	0.57 nN/nm$^{0.53}$
n	0.97
E_{eff}^{HS}	10^2 MPa
E_{eff}^{HC}	1.46 MPa
h	529 nm
$\delta_{lc,2}$	14.01 nm
$\delta_{lc,3}$	0 nm
$\delta_{uc,1}$	14.01 nm
$\delta_{uc,2}$	δ_{max} = 34.03 nm

Figure 6 depicts an example FIC for PDMS. The MRA provides adequate fitting throughout the entire range of indenter displacement. From the location of the critical limits, two regimes are obtained; the first one consists of a serial arrangement of resistors 1 and 3 (surface forces and elastic thin film) and the second of a serial arrangement of resistors 2 and 3 (elastic solid and elastic thin film). The presence of two regimes in the FIC is in fact evident from direct inspection of the log-log curve, as illustrated by the piece-wise linear fit (blue line) although the MRA determines that these arise from 3 different resistors. From visual analysis, the line spanning from δ_m = 2 nm to δ_m = 14 nm has a slope of 1.61. The slight departure from 1.5 can be accounted for in the MRA by a *realistic* non-zero displacement offset, δ_0. If $F \propto (\delta_m + \delta_0)^{3/2}$, it is only for $\delta_m >> \delta_0$ that the log-log curve asymptotically approaches a slope of 1.5. The appropriate combination of resistors using MRA predicts the measured slope. The full set of fitting parameters for this particular curve is summarized in Table 1. Notice that $E_{eff}^{HS} = 10^2$ MPa $>> E_{eff}^{HC} = 1.46$ MPa, which means the Hertzian resistor essentially does not deform. This does not mean the substrate supporting the film is rigid; it simply means that a maximum indentation of 36.1 nm does not produce a significant deformation of the substrate, given a film thickness of 529 nm. On the other hand, while the maximum indentation is small compared to the thickness of the film, it is considerable enough to have the FIC modelled as a thin film rather than an elastic solid because of the large radius of the indenter (χ > 1 at maximum depth).

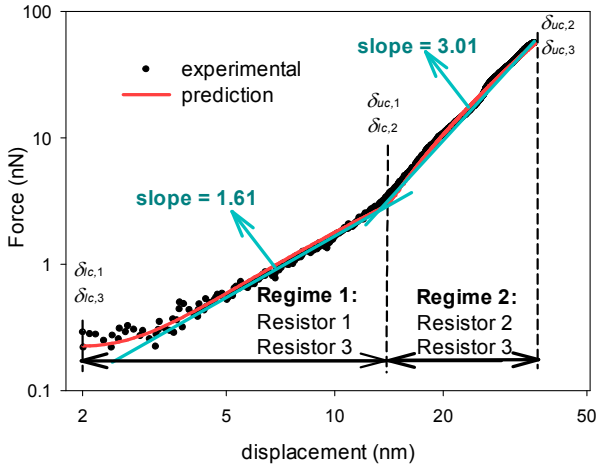

Figure 6. Example FIC of PDMS with a spherical indenter. The MRA provides adequate fitting throughout the entire range of indenter displacement. As a reference, the green line represents the best two-regime linear fit of the plot, with slopes 1.6 and 3.0 respectively. Comparing this Figure and Figure 4C, it is clear there is not necessarily a correlation between the number of mechanical resistors and regimes.

Figure 7 compares the values of the Young's modulus obtained through several methods by fitting experimental FIC data using:

- Oliver-Pharr (OP)[27] model using $dP/dh = 2\sqrt{R_{tip} E_{eff} \delta_{max}}$;
- Hertz-Chadwick (HC) [8, 9] model for final portion of the FIC (asymptotic fit);
- HC model for the full FIC (full FIC fit).

In addition, it includes fitting of the linear region of the force-strain curve from uniaxial extension testing (UA), measured on a bulk elastomer.

Table 2. Average values of Young's modulus and standard deviations extracted using Hertz-Chadwick (HC) model [47],

Oliver-Pharr (OP) model [27], and the MRA method for PDMS indented with a 10.5 μm spherical probe.

Method	Mean (MPa)	Standard deviation (MPa)
MRA	1.52	0.50
HC - full FIC fit	0.74	0.22
OP (log-log slope < 3)	2.00	0.41
HC–asymptotic (log-log slope < 3)	2.10	0.43
UA	1.45	0.50

An increase in the predicted modulus with maximum indentation depth is observed in all indentation models, but particularly in those involving asymptotic fitting. However, if δ_{max} is taken as the point at which the log-log slope of the FIC reaches 3, a mean modulus of 2 MPa is obtained with a small standard deviation (0.41) using OP. The OP model yields results with the lowest standard deviation among the different methods (see Table 2) when a maximum slope of 3 is specified. However, if curves are analysed without checking for the slope at the position of the maximum, then the standard deviation exceeds that from MRA by a factor of 4; this is understandable since MRA performs an automatic check of regime applicability with respect to the range of power law exponents. The OP model results in a higher modulus compared to the MRA, while full fitting with the HC model gave lowest values of the elastic modulus, probably due to influence from the surface forces.

The MRA yielded values closest to the bulk values of elastic modulus, which can be considered as a successful criterion that validates the routine. We note that the good correlation between the bulk and MRA nanoindentation moduli is not due to a larger number of fitting parameters handled by the MRA model; on the contrary, the large number of parameters is usually less reliable since it increases the chance of non-unique combinations of parameters to satisfy the fit. The lower standard deviations and the corresponding consistency of the results do, however, benefit from multiple parameters that enable it to accommodate multiple scenarios of the indentation process. It should be noted that the modulus obtained using MRA is that from the thin film, which turned out to be the most adequate to describe the indentation of the elastomer's surface. UA is, on the other hand, a bulk measurement performed over a 1 cm thick strip that is likely unaffected by the presence of a 0.5 μm surface layer. The surface layer is likely a swollen, hydrated layer of PDMS exhibiting viscoelastic behavior that is not intrinsic to the elastomer but a consequence of water diffusion (poroelasticity) [48]. If the time-dependent response vanishes quickly (which is reasonable for such small penetrations), the equilibrium modulus converges to the bulk modulus, explaining the excellent agreement between MRA and UA data over the indentation range 15 nm to 50 nm. For a maximum depth below ~15 nm, under-prediction is not surprising due to the dominance of the surface forces.

3.4 Analysis of FI curves for *Lolium multiflorum* cells

The choice of plant-based systems as a biological model was dictated by the innate features of plant cells that have multiple structural elements with distinct mechanical properties. [2, 3] Typically, the micromechanical properties are examined by collecting a 2D array of force curves over an area of interest. Such an array, also called a force volume plot, can be then used to present results in a graphical format as an image or a 3D contour plot. For the purposes of testing the MRA routine, however, we required high spatial density of force curves to ensure that any point-to-point variations are associated with the material properties and not with experimental or analysis artefacts. Thus, instead of a 2D array we have recorded numerous 1D tracks with 2-3 curves per point and with about 100-300 curves per track. By doing so, we ensured that the distance between points is less than ~2-4 times the radius of the tip.

In Figure 8, typical FICs for *L. multiflorum* suspension-cultured cells are presented, together with fitting lines produced using the MRA routine. We generally observed little or no adhesion, although at certain locations on the cell surface we recorded multiple detachment peaks consistent with stretching of surface bound polymers, which we expect to be from the non-cellulosic polysaccharides (mostly hemicelluloses in this case). The analysis of these adhesive interactions has been already successfully realised within an automated routine [49], and hence was out of the scope of the current paper. Fig. 8

shows a hysteresis between the approach and retract curves, which is significantly larger than that observed for PDMS. The average energy dissipated during the indentation cycle, $E_{Dissipated} = \int_0^{\delta_{max}} (F_{approach} - F_{retract}) d\delta$, is found to be 69(±6.7s.e.)·10^{-18} J per indentation cycle. The degree of hysteresis for the plant cells varied significantly, with the minimum and maximum values of 1.59·10^{-21} J and 0.7·10^{-15} J respectively.

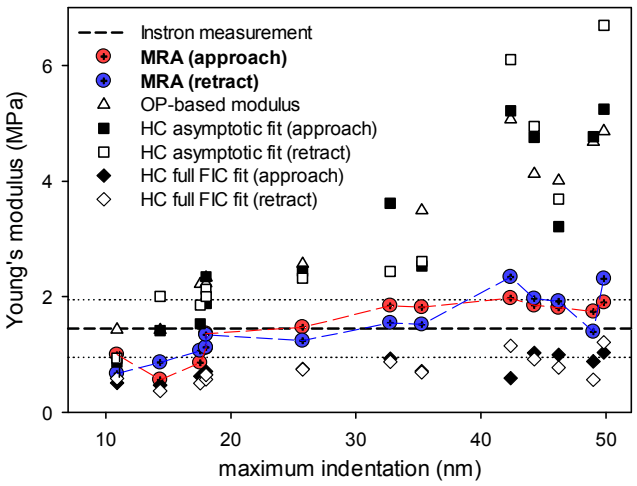

Figure 7. MRA was validated by comparing the Young's modulus of PDMS obtained through MRA interpretation of AFM nanoindentation and that from uniaxial stretching (UA) experiments. For indentations above 15 nm, the MRA predicts modulus values that are highly consistent with the bulk modulus from UA measurements (generally within one standard deviation shown by dashed-dot lines) and there is no apparent dependence on indentation depth. The OP and HC based moduli were also computed. The OP-based modulus is similar to that obtained from the asymptotic fit of the FIC using the HC model, with values increasing with indentation depth. Fitting the entire curve with HC produces consistent underprediction of the bulk modulus, as a consequence of the influence of surface interactions.

The values of fitting parameters for the entire dataset are summarized in Table S1 (Supplementary Information). The majority of datasets recorded for *L. multiflorum* cells using an AFM tip displayed a behavior characterized by three resistors: a surface force, linear deformation (a quasi-'elastic shell') and a thin elastic film. The linear deformation normally occurred concomitantly with the other resistors, creating a two regime response. A significant number of curves had some discontinuities that are likely to be associated with the penetration of the tip into voids within the polysaccharide mesh of the cell wall. Since large discontinuities may cause considerable error in parameter estimation if not taken into account, the algorithm is allowed to produce as many discontinuities as there are regime transitions, given that it is in these instances that the largest discontinuities are found. Still, the presence of discontinuities is the most challenging aspect to be handled during curve fitting and more rigorous approaches to incorporate them need to be developed.

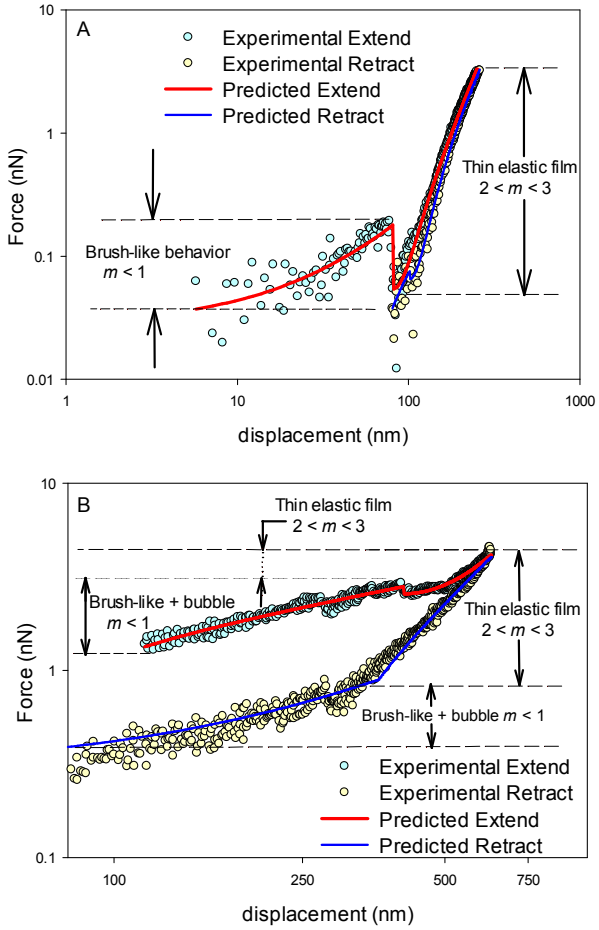

Figure 8. Typical FICs for *L. multiflorum* suspended culture cells. The majority of FICs were characterized by three resistors: a surface force (**A** and **B**), a quasi-'elastic shell' or 'bubble' (**B** only) and a thin elastic film (**A** and **B**). The 'bubble' in **B** occurred concomitantly with the other resistors, generating a two regime response. In both cases, discontinuities associated with penetration of the tip into the voids of the cell wall polysaccharide mesh are present.

To compare the performance of MRA, OP and HS models, we used 1D datasets collected on *L.multiflorum* cells. Figures 9A and B depict the parameters obtained

from interpretation of indentation data taken along an arc trajectory (3 μm long) on the surface of the cell. Firstly, we found that the average difference between the moduli calculated from the approach and retract branches is 1.1 MPa for the HS model, considerably higher than that found for the MRA method of 0.3 MPa. The good correlation between the moduli obtained from approach and retract curves using MRA is better appreciated in Figure 9C, where it is clear that superior consistency is achieved compared to HS. The large differences between approach and retract observed in HS are associated with the cross-talk between surface forces and the elastic part of the indentation curve. This may arise from the weak brush-like interactions that are evident on the approach branch before the tip makes full contact with the cell wall, which the HS model attributes entirely to a soft Hertzian film/solid, leading to an approach modulus considerably lower than obtained from the retract branch. Such an effect is not observed for PDMS because surface roughness is expected to be more pronounced for the locally disordered and highly heterogeneous surface of a plant cell. On the other hand, the high modulus from the retract curve using HS is a consequence of the presence of highly non-linear segments, with large values of the power law exponent. In MRA such segments are accounted for by using an empirical hyperelastic model. The OP fitting was performed by truncating the curve when its log-log slope was above 3, which means this method does not suffer from the presence of higher order regimes. Among all the methods compared in Figure 9, OP is the one with the lowest averaged-standard deviation (i.e. the average of the standard deviations at every point) and follows closely the trend obtained through MRA. However, since OP is entirely based on analysis of the retract curve, it is not possible to check its consistency.

We also note that the discrepancy in the values of the modulus obtained through MRA (~2MPa) and OP (~0.5MPa) is not due to a potential correlation between thickness and elastic modulus, which is a recognized issue in the thin film model by Chadwick and co-workers [8, 9]. Simultaneous determination of the modulus and wall thickness from AFM measurements is a challenging task, and similar issues are recognized for indentation of plant cells with a macroscopic flat punch [50]. Fortunately, the thin film deformation region is only ~100-300 nm in thickness, which is a fraction of the total indentation and much smaller than the thickness of L.multiflorum cell walls (ca. 1000-3000 nm according to microscopy measurements[51]). Therefore, a 10% error in wall thickness results in only a 1% error in elastic modulus, provided indentation-thickness ratio stays ≤0.1, i.e. $\frac{\Delta E}{E} \sim \frac{\delta_{Thin\ Film}}{h}\left(\frac{\Delta h}{h}\right) \sim 0.1\frac{\Delta h}{h}$.

These results demonstrate the power of the MRA to reasonably interpret complex and non-linear FICs obtained during approach and retraction of an AFM cantilever. The method is particularly powerful for biological samples that display significant hysteresis between approach and retract, thereby providing superior quantification of micromechanical properties over the routinely used OP and HS models.

4 Conclusions

A Multi-Regime Analysis (MRA) has been developed as a new routine for analysing complex force indentation measurements from the AFM. This analysis provides, for the first time, a simple means in which to obtain relevant micromechanical properties of materials where there are multiple contributions to mechanical response in force-indention experiments. The advantage of the approach is that it enables non-linear FICs to be interpreted using several contact micromechanics models, and ensures that these models are used within their relevant ranges of applicability. Another major advantage of the MRA approach, particularly for naturally variable biological systems, is that the MRA can be routinely used to analyse large data sets of FICs, even when they contain several deformation regimes as is the case for complex soft materials such as cells. The key feature of the analysis, as applied here, is that it resolves convoluted force-indentation curves by assuming the force-indentation response is a result of the serial superposition of elastic resistors, each operating within a well-defined range of deformations.

The MRA algorithm is demonstrated to accurately interpret nano-indentation measurements performed on PDMS microspheres. We find this approach allows

identification of three major contributors to the micromechanical response of the spheres; surface force, an elastic thin film and elastic solid. It uniquely obtains an elastic modulus that is similar to the bulk elastic modulus of the PDMS. In comparison, the OP model results in significantly higher modulus than the bulk value while the HC model under predicted its value; these regularly used models are unable to account for multiple contributions to the measured mechanical response.

The MRA is used in an automated routine to analysis plant cells to show that their micromechanical response arises from a combination of surface forces, a stiff cell wall, and a Hertzian thin film. We discover that the MRA approach uniquely predicts the same modulus of the cell wall from both approach and retraction curves, which further validates the MRA model. Since plant cells, like many other biological systems, are inherently heterogeneous, the advantage of a MRA is that it is readily automated to allow large sets of FIC curves at multiple locations around a cell, and/or on multiple cells, to be routinely analysed. We use this method to identify that there are local variations in the mechanical parameters of plant cell walls, which may be relevant to cell growth and require further research; this new technique will allow such research to be possible.

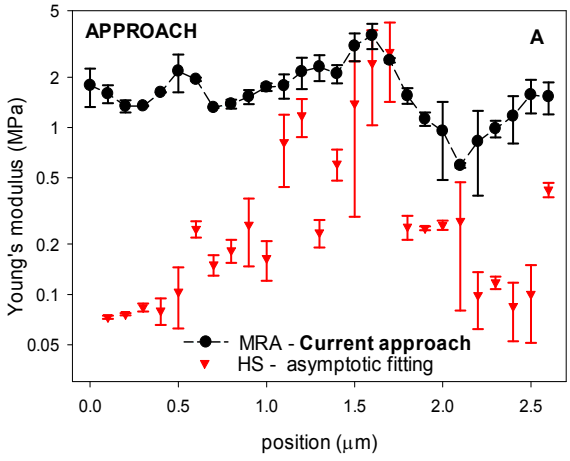

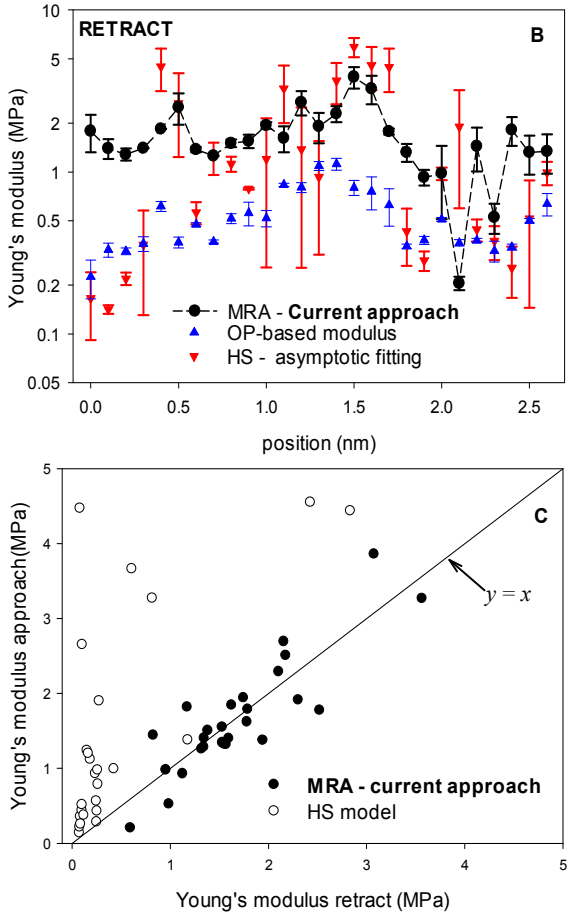

Figure 9. Validation of MRA through interpretation of AFM nanoindentation experiments on plant cells. The plots compare 1D track elastic moduli calculated from MRA, OP and HS. Two repetitions per point were performed; the symbols represent the average value and the bars standard deviation during (A) Approach and (B) Retract. The OP fitting was performed by truncating the curve when its log-log slope was above 3. (C) Correlation between elastic moduli extracted from Approach and Retract branches of the force curve through HS and MRA. The strong correlation displayed by the MRA-based moduli strongly supports the validity of the technique. On the other hand, HS produces approach and retract moduli that greatly deviates for the $y = x$ line.

We consider that the MRA approach will add significant value to recent technique developments for the AFM, including research that combines linear indentation with oscillatory measurements, such as multi-harmonic analysis [52], Amplitude-Modulated-Frequency-Modulated AFM [53], or PeakForce tapping QNM® (Quantitative Nanomechanical Property Mapping) [54]. The essential principle of oscillatory methods is that they analyse changes in the Fourier spectrum of the AFM cantilever oscillations upon interaction with the cell surface. Further,

the spectrum parameters can be related to local mechanical properties of the surface [55, 56] and hence can probe high frequency viscoelastic response that is inaccessible in liner indentation measurements, and therefore provides important complimentary information.

In conclusion, Multi-Regime Analysis extracts new information from AFM indentation measurements by disentangling different mechanical contributions convoluted within a force-versus indentation curve. The extraction of conventional elastic parameters such as Young's modulus yielded high consistency, thus leading to a more accurate and precise nanomechanical mapping of biological materials using AFM. The method can be easily extended and adapted to include viscoelastic and plastic regimes. The method provides an important first approximation tool in discovering underlying mechanisms of mechanical behaviour in biological systems, and is essential for interpreting force-indentation measurements of such systems and other soft materials with hierarchical structures.

Acknowledgements

This work was performed in part at the Queensland node of the Australian National Fabrication Facility, a company established under the National Collaborative Research Infrastructure Strategy to provide nano- and micro-fabrication facilities for Australia's researchers. In particular, Dr Elena Taran is acknowledged for invaluable help with setting up AFM experiments. Mr William McCumstie is acknowledged for his pivotal contribution at the early stages of the development of the MATLAB code. Mr Tony Chin, Dr Kim Johnson and Dr Monika Doblin of The University of Melbourne are gratefully acknowledged for providing the Lolium multiflorum cell cultures Dr Huaying Chen is gratefully acknowledged for sharing the micro-well cell entrapment method ahead of publication and his help with fabrication, design development and helpful discussions. Dr Bogdan Donose is gratefully acknowledged for many helpful discussions. Drs. Grant Edwards and Patricia Lopez-Sanchez are gratefully acknowledged for their help with the Instron measurements. The ARC Centre of Excellence in Plant Cell Walls is acknowledged for financial support.

Notes and references

[a] ARC Centre of Excellence in Plant Cell Walls, School of Chemical Engineering, The University of Queensland, Brisbane, Australia.
[b] School of Chemical Engineering, The University of Queensland, Brisbane, Australia.
[c] ARC Centre of Excellence in Plant Cell Walls, Centre for Nutrition and Food Sciences, Queensland Alliance for Agriculture and Food Innovation, The University of Queensland, Brisbane, Australia.
* Corresponding author: g.yakubov@uq.edu.au

† Author Contributions: G.Y. designed and performed the nanoindentation experiments, and introduced the idea of a multi-regime analysis algorithm. M.R.B. and G.Y. jointly developed the analytical part of the multi-regime analysis routine, M.R.B. wrote and implemented the Multi-Regime Analysis computer routine and analysed experimental data. J.R.S. contributed expertise in soft matter and micromechanics, as well as providing guidance on experimental methods, results interpretation and model implementation. M.G. contributed expertise in plant biology and plant mechanics. G.Y. and M.R.B. wrote the manuscript together with contributions from J.S. and M.G. All authors discussed the results and commented on the manuscript.

Electronic Supplementary Information (ESI) available: Supplementary Information contains specific AFM considerations, as well as additional implementation details regarding curve interpolation and comparisons of fitting in linear and log-log scale. Fitting parameters for the entire dataset of indentations of *L. multiflorum* cells with a conical indenter are also provided. See DOI: 10.1039/b000000x/

1. D. J. Mueller and Y. F. Dufrene, *Nature Nanotechnology*, 2008, **3**, 261-269.
2. A.-L. Routier-Kierzkowska and R. S. Smith, in *Plant Cell Morphogenesis: Methods and Protocols*, eds. V. Zarsky and F. Cvrckova, 2014, vol. 1080, pp. 135-146.
3. A.-L. Routier-Kierzkowska, A. Weber, P. Kochova, D. Felekis, B. J. Nelson, C. Kuhlemeier and R. S. Smith, *Plant Physiology*, 2012, **158**, 1514-1522.
4. V. V. Lulevich, D. Andrienko and O. I. Vinogradova, *Journal of Chemical Physics*, 2004, **120**, 3822-3826.
5. K. D. Costa, A. J. Sim and F. C. P. Yin, *Journal of Biomechanical Engineering-Transactions of the Asme*, 2006, **128**, 176-184.
6. R. C. Batra and W. Jiang, *International Journal of Solids and Structures*, 2008, **45**, 5814-5830.
7. Z. Y. Ai, Z. Q. Yue, L. G. Tham and M. Yang, *International Journal of Engineering Science*, 2002, **40**, 1453-1483.

8. E. K. Dimitriadis, F. Horkay, J. Maresca, B. Kachar and R. S. Chadwick, *Biophysical Journal*, 2002, **82**, 2798-2810.
9. N. Gavara and R. S. Chadwick, *Nature Nanotechnology*, 2012, **7**, 733-736.
10. Y. C. Gao and T. J. Gao, *International Journal of Solids and Structures*, 2000, **37**, 4319-4334.
11. Y. F. Cao, D. H. Yang and W. Soboyejoy, *Journal of Materials Research*, 2005, **20**, 2004-2011.
12. Z. Chen, S. Diebels, N. J. Peter and A. S. Schneider, *Computational Materials Science*, 2013, **72**, 127-139.
13. F. Yang, *Journal of Materials Research*, 2006, **21**, 2683-2688.
14. D. M. Ebenstein, *Journal of Materials Research*, 2011, **26**, 1026-1035.
15. J. C. Kohn and D. M. Ebenstein, *Journal of the Mechanical Behavior of Biomedical Materials*, 2013, **20**, 316-326.
16. S. Yang, Y. W. Zhang and K. Y. Zeng, *Journal of Applied Physics*, 2004, **95**, 3655-3666.
17. P. Attard, *Journal of Physics-Condensed Matter*, 2007, **19**.
18. G. Gillies, C. A. Prestidge and P. Attard, *Langmuir*, 2002, **18**, 1674-1679.
19. M. E. Dokukin, N. V. Guz and I. Sokolov, *Biophysical Journal*, 2013, **104**, 2123-2131.
20. I. Sokolov, M. E. Dokukin and N. V. Guz, *Methods*, 2013, **60**, 202-213.
21. R. A. Burton, M. J. Gidley and G. B. Fincher, *Nat Chem Biol*, 2010, **6**, 724-732.
22. S. T. Milner, T. A. Witten and M. E. Cates, *Macromolecules*, 1988, **21**, 2610-2619.
23. J. C. Xia, R. P. Daly, F. C. Chuang, L. Parker, J. H. Jensen and C. J. Margulis, *Journal of Chemical Theory and Computation*, 2007, **3**, 1629-1643.
24. A. Boccaccio, M. C. Frassanito, L. Lamberti, R. Brunelli, G. Maulucci, M. Monaci, M. Papi, C. Pappalettere, T. Parasassi, L. Sylla, F. Ursini and M. De Spirito, *Journal of The Royal Society Interface*, 2012.
25. J. Arfsten, C. Bradtmöller, I. Kampen and A. Kwade, *J. Mater. Res.*, 2008, **23**, 3153-3160.
26. F. Huang, H. Qiu and W. Guo, *Sci. China Technol. Sci.*, 2014, **57**, 706-712.
27. W. C. Oliver and G. M. Pharr, *Journal of Materials Research*, 1992, **7**, 1564-1583.
28. M. J. Higgins, R. Proksch, J. E. Sader, M. Polcik, S. Mc Endoo, J. P. Cleveland and S. P. Jarvis, *Review of Scientific Instruments*, 2006, **77**.
29. J. E. Sader, J. A. Sanelli, B. D. Adamson, J. P. Monty, X. Wei, S. A. Crawford, J. R. Friend, I. Marusic, P. Mulvaney and E. J. Bieske, *Review of Scientific Instruments*, 2012, **83**.
30. M. M. Smith and B. A. Stone, *Australian Journal of Biological Sciences*, 1973, **26**, 123-133.
31. G. E. Yakubov, J. McColl, J. H. H. Bongaerts and J. J. Ramsden, *Langmuir*, 2009, **25**, 2313-2321.
32. O. I. Vinogradova, H. J. Butt, G. E. Yakubov and F. Feuillebois, *Review of Scientific Instruments*, 2001, **72**, 2330-2339.
33. O. I. Vinogradova and G. E. Yakubov, *Langmuir*, 2003, **19**, 1227-1234.
34. H. Chen, J. Li, H. Zhang, M. Li, G. Rosengarten and R. E. Nordon, *Biomicrofluidics*, 2011, **5**.
35. A. N. Fernandes, X. Chen, C. A. Scotchford, J. Walker, D. M. Wells, C. J. Roberts and N. M. Everitt, *Physical Review E*, 2012, **85**.
36. J. McColl, G. E. Yakubov and J. J. Ramsden, *Langmuir*, 2007, **23**, 7096-7100.
37. X. D. Li and B. Bhushan, *Materials Characterization*, 2002, **48**, 11-36.
38. F. Rico, P. Roca-Cusachs, N. Gavara, R. Farre, M. Rotger and D. Navajas, *Physical Review E*, 2005, **72**.
39. A. Touhami, B. Nysten and Y. F. Dufrêne, *Langmuir*, 2003, **19**, 4539-4543.
40. J. M. Watson and M. G. Baron, *Journal of Membrane Science*, 1996, **110**, 47-57.
41. C. A. Charitidis, *Industrial & Engineering Chemistry Research*, 2011, **50**, 565-570.
42. C. A. Charitidis, E. P. Koumoulos, V. P. Tsikourkitoudi, D. A. Dragatogiannis and G. Lolas, *Plastics Rubber and Composites*, 2012, **41**, 94-99.
43. P. Milani, M. Gholamirad, J. Traas, A. Arneodo, A. Boudaoud, F. Argoul and O. Hamant, *Plant Journal*, 2011, **67**, 1116-1123.
44. C. X. Wang, L. Wang and C. R. Thomas, *Annals of Botany*, 2004, **93**, 443-453.
45. N. Q. Wu and M. J. Pitts, *Postharvest Biology and Technology*, 1999, **16**, 1-8.
46. Y. R. Silberberg, G. E. Yakubov, M. A. Horton and A. E. Pelling, *Nanotechnology*, 2009, **20**.
47. I. N. Sneddon, *International Journal of Engineering Science*, 1965, **3**, 47-57.
48. Y. Hu, X. Chen, G. M. Whitesides, J. J. Vlassak and Z. Suo, *Journal of Materials Research*, 2011, **26**, 785-795.
49. P. Polyakov, C. Soussen, J. Duan, J. F. L. Duval, D. Brie and G. Francius, *Plos One*, 2011, **6**.
50. A. E. Smith, K. E. Moxham and A. P. J. Middelberg, *Chemical Engineering Science*, 1998, **53**, 3913-3922.
51. P. R. Moghaddam and D. Wilman, *Journal of Agricultural Science*, 1998, **131**, 59-67.
52. A. Raman, S. Trigueros, A. Cartagena, A. P. Z. Stevenson, M. Susilo, E. Nauman and S. A. Contera, *Nature Nanotechnology*, 2011, **6**, 809-814.
53. R. R. Proksch, I.; Hohlbach, S.; Cleveland, J.; Geisse, N.; Moshar, A.; Bemis, J.; Callahan, C., presented in part at the NSTI/Nanotech Santa Clara, CA, USA, June 21, 2012.
54. D. A. Lamprou, V. Venkatpurwar and M. N. V. R. Kumar, *Plos One*, 2013, **8**.
55. M. E. Dokukin and I. Sokolov, *Langmuir*, 2012, **28**, 16060-16071.
56. C. M. Hayot, E. Forouzesh, A. Goel, Z. Avramova and J. A. Turner, *Journal of Experimental Botany*, 2012, **63**, 2525-2540.